We are IntechOpen, the world's leading publisher of Open Access books
Built by scientists, for scientists

6,900
Open access books available

185,000
International authors and editors

200M
Downloads

Our authors are among the

154
Countries delivered to

TOP 1%
most cited scientists

12.2%
Contributors from top 500 universities

WEB OF SCIENCE™

Selection of our books indexed in the Book Citation Index
in Web of Science™ Core Collection (BKCI)

Interested in publishing with us?
Contact book.department@intechopen.com

Numbers displayed above are based on latest data collected.
For more information visit www.intechopen.com

Chapter

Surface Plasmons and Optical Dynamics on Vanadium Dioxide

Hiroaki Matsui

Abstract

We report on plasmonic resonances on VO_2 nanodot arrays and associated optical dynamics. The plasmon excitations based on electric field interactions lead to red shifts of the plasmon resonances to lower photon energy with increasing nanodot size. The spectral linewidths of plasmon peaks gradually become narrow with increasing nanodot size. This is related to a reduction in plasmon damping with respect to the electronic band structure of VO_2. This specific band structure of VO_2 affects the optical dynamics of plasmon resonances at the sub-picosecond scale. The optical excitations of VO_2 comprise intraband and interband transitions. The existence of plasmon bands induces long-lived lifetimes on decay processes. Intraband transitions in the conduction band (C.B.) play an important role in producing long lifetimes, attributing to free carriers in the C.B. By contrast, interband transitions related to bound electrons contribute to plasmon damping. The dynamic optical responses are closely related to the electronic band structures of VO_2.

Keywords: VO_2, surface plasmon, infrared, dynamics, Mott insulator

1. Introduction

Recently, plasmonic materials based on oxide and compound semiconductors (e.g., ZnO, CuSe, and InN) have received much attention given that plasmonic responses can be tuned by external fields [1–5]. Investigation of these materials has led to the identification of a new family of plasmonic materials in the infrared (IR) range, which differ from noble metals (e.g., Ag and Au) that have fixed free electron densities. Oxide and compound semiconductors show ideal Drude terms in the IR range due to the absence of interband transitions in the band gap [6]. Plasmonic tuning can be effected by carrier injections due to control of the Fermi level in the electronic bands [7, 8]. The optical features arising from these emerging plasmonic semiconductors show promise for use in optical applications in the IR range.

Control of free carriers has been reported on oxide materials with strong electron-electron correlations. Of these, materials comprising vanadium dioxide (VO_2) show a sharp insulator-metal transition (IMT) based on Mott-related and Peierls-related processes [9], which can be controlled by external fields such as thermal, electrical, and optical inputs. In particular, dramatic change of the specific band structure of VO_2 with external fields provides more than a three orders of magnitude change in electrical conductance. The IMT character of VO_2 resulting

from the spin-orbital interactions makes this material a candidate for use in optoelectronic applications [10–13]. The widespread interest in VO_2 has further focused on elucidating the complicated domain and grain structures in the vicinity of IMT. This determines the spatial and hysteretic nature of the phase transition of VO_2. Recent studies have reported optical phenomena from plasmonic structures of VO_2 with nanostructures such as nanodots and nanoparticles in an effort to understand the correlation between the optical response and phase transition [14–17]. These investigations have fueled further interest in nanostructures of VO_2 and are a very exciting and promising area of research with respect to active plasmonic materials.

The ultrafast dynamics of free carriers in metals have received much attention. Above all, photo-induced alternation of the plasmonic response is a powerful tool in the fabrication of optically controlled nanophotonic devices. The combination of ultrafast optical manipulations with large reflectance and transmittance is expected to yield promising results in applications concerning active plasmonics and optical switching [18, 19]. Thus far, plasmon modulations at the sub-picosecond scale have been reported on noble metals such as gold and silver, being the most commonly adopted plasmonic materials [20]. In general, effort aimed at exploiting ultrafast dynamics requires the production of intense concentrations of energy (hot electrons and hot holes) in the hosts. The dipolar excitations of all free carriers in plasmonic resonances have large extinction cross-sections, which can easily concentrate light into nanoscopic volumes. These phenomena have been utilized in furthering the development of certain areas of photo-chemistry such as photo-catalytic reactions and surface-enhanced Raman scattering (SERS).

Recently, investigations of the optical dynamics of oxide semiconductors have focused on Sn-doped In_2O_3 and Ga-doped ZnO [21, 22]. The noble metals have large amounts of free electrons in the host. Their plasmonic characters are hardly tunable. By contrast, oxide materials can be easily controlled by optical excitations such as intraband and interband transitions. For example, an interband transition is based on carrier excitation between the conduction band (C.B.) and valence band (V.B.), which can markedly change the plasma frequency that is dependent on carrier concentration, leading to an optical tuning of a plasmon response. However, an optical dynamics on an interband transition are known to show long plasmon lifetimes of several picoseconds. On the other hand, a carrier excitation (electron or hole) in the C.B. or V.B. is based on an intraband transition, resulting in significantly faster plasmon lifetimes at the sub-picosecond scale [23]. Therefore, oxide semiconductors are expected to show ultrafast optical modulations. Unfortunately, the plasmon dynamics of VO_2 have hitherto not been investigated. The electronic band structure of VO_2 differs largely from that of oxide semiconductors, which show different optical dynamics due to the strong electron-electron correlations of $3d$ bands.

In this chapter, we highlight the surface plasmons and associated optical dynamics of VO_2 with two-dimensional (2D) nanodot arrays. Periodic alignments of metallic nanodots can excite collective plasmon resonances due to electromagnetic coupling between nanodots that are in close proximity. This plasmon coupling in the nanodot arrays markedly influences the optical excitation and resonant energy. In the first section, we introduce surface plasmons of VO_2 nanodot arrays and their damping processes, which will contribute toward our understanding of ultrafast dynamics of plasmon resonances. In the second section, we report on the optical dynamics of VO_2 nanodot arrays by the plasmonic excitations based on intraband transitions of C.B. Ultrafast optical modulations are observed in VO_2 nanodot arrays at the sub-picosecond scale. This work provides new insight into plasmon-induced optical dynamics of VO_2.

2. Surface plasmons of VO₂ nanodot arrays

2.1 Fabrication of nanodot arrays

VO$_2$ nanodot arrays were fabricated by top-down processes as follows [24]. VO$_2$ films were epitaxially grown on Al$_2$O$_3$ (0001) substrates at a substrate temperature of 420°C using pulsed laser deposition. ArF laser pulses were focused on VO$_2$ targets in an oxygen atmosphere of 1.0 Pa. After growing VO$_2$ films, a UV nanoimprint resist with a thickness of 200 nm was spin-coated onto VO$_2$ film surfaces. The lithography process was performed using an UV lithography system to fabricate the nanodot array structure. The coated resists were pushed by quartz molds with UV transparency under a pressure of 3 MPa for 5 min. The residual resist on the VO$_2$ film surfaces after processing the UV lithography was removed by O$_2$ plasma irradiation. Additionally, reactive ion etching (RIE) using SF$_6$ plasma was used to process VO$_2$ films to obtain nanodot arrays. SF$_6$ RIE was conducted under an input of 60 W and a gas pressure of 1 Pa for 30 s. The resist layers that remained on VO$_2$ nanodot arrays were removed in toluene for completion of the VO$_2$ nanodots.

Figure 1 shows X-ray 2θ diffraction (XRD) patterns of VO$_2$ nanodot array samples with different sizes (*D* = 340, 600, and 816 nm). XRD patterns with the (020) diffraction plane are only shown. The patterns indicated a monoclinic structure corresponding to a low temperature phase of VO$_2$. The 490- and 716-nm nanodot array samples also exhibited similar XRD patterns.
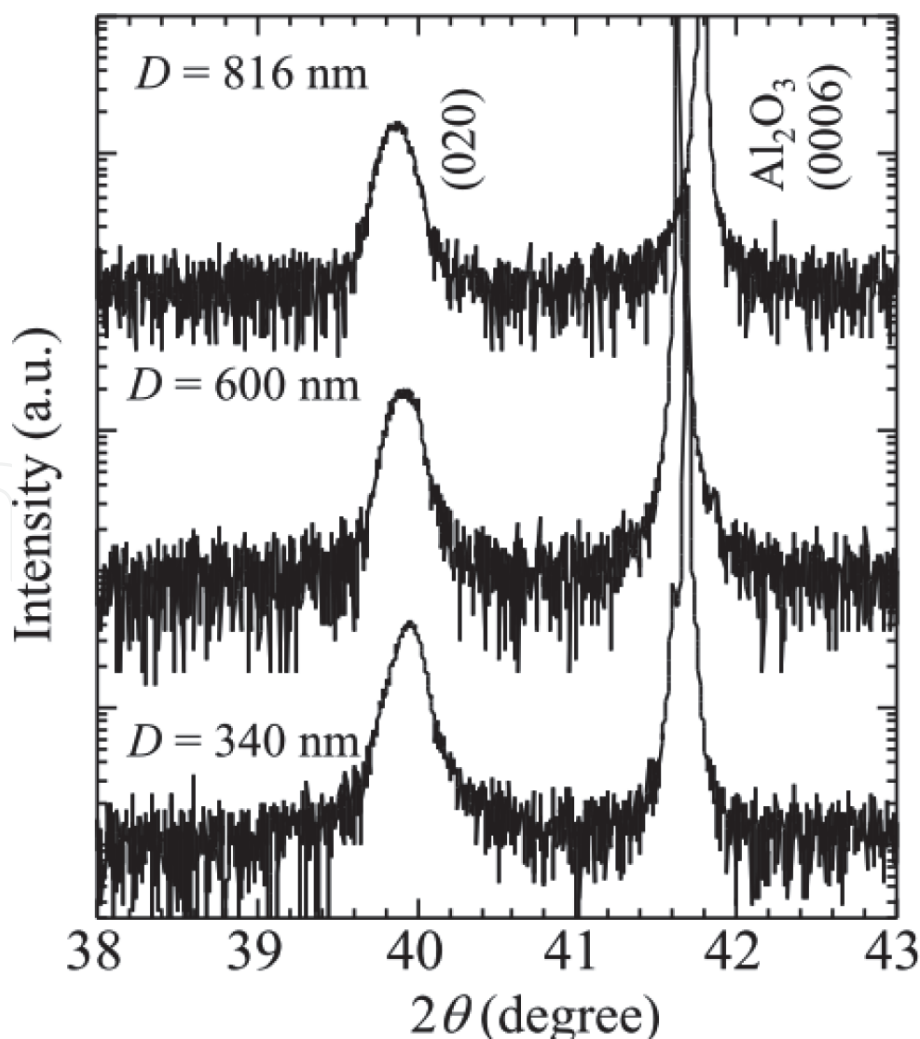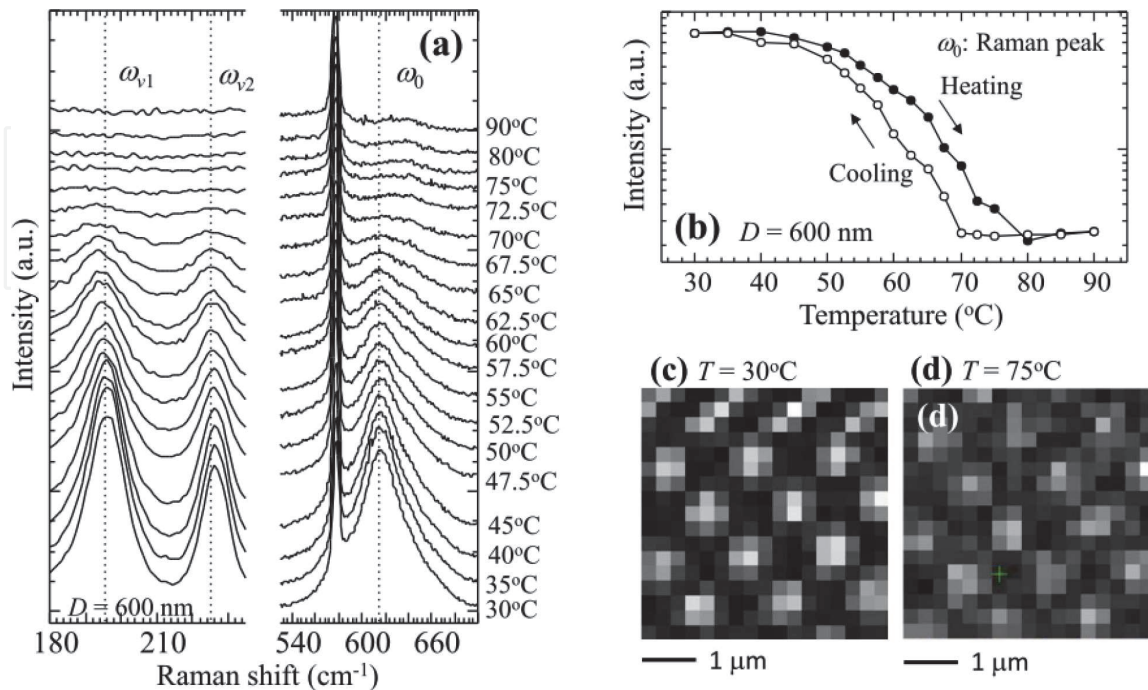

Figure 1.
*2θ XRD patterns of VO$_2$ nanodot arrays with different sizes (D = 340, 600, and 816 nm) [24].*

Temperature-dependent Raman measurements were investigated in an effort to identify structural changes in the VO_2 nanodot arrays (**Figure 2a**). The Raman peaks at 195, 224, and 614 cm^{-1} were mainly attributed to V-V (ω_1 and ω_2) and V-O (ω_o) vibrational modes, respectively [25]. Raman studies play an important role in clearing structural changes during the IMT, which is the index of our understanding regarding hysteresis phenomena of plasmon resonances. The peak at 195 cm^{-1} showed a slight change at 60°C. An additional peak at 632 cm^{-1} was detected above 60°C in the vicinity of the peak at 614 cm^{-1}. Insulating phases in VO_2 have the monoclinic M_1 and M_2 and triclinic T phases [26]. The M_2 phase is distinguished from the M_1 phase primarily by the red shift of the ω_o frequency [25]. **Figure 2a** shows that the M_1 phase at 60°C nucleated between the growing metallic rutile R phase and the remaining M_1 phase. The M_2 and R phases grew until the M_1 phase was consumed at this temperature and the R phase began to consume the M_2 phase. Furthermore, the transition to the R phase was complete at around 75°C. The hysteresis curve of the ω_0-related Raman peak shows that the hysteresis width was very broad (**Figure 2b**). Finally, we confirmed Raman peaks related to each nanodot using micro-Raman spectroscopy. All nanodots showed similar Raman spectra and associated temperature dependencies (**Figure 2c, d**). The XRD and Raman measurements revealed that the VO_2 nanodot arrays were well fabricated with high crystallinity.

2.2 Plasmon resonances and field distributions

Figure 3 shows the experimental and simulated extinction (A) spectra of VO_2 nanodot arrays with different sizes (D) from 340 to 816 nm, as characterized by $A = -\log_{10}(\text{transmittance})$. All samples were observed at 90°C in order to monitor plasmon resonances of the nanodot arrays. Extinction spectra were employed using two types of optical measurement systems. One comprised a Vis-NIR spectra from 2500 to 400 nm and the other is a FTIR spectra from 8000 to 4000 cm^{-1}. The
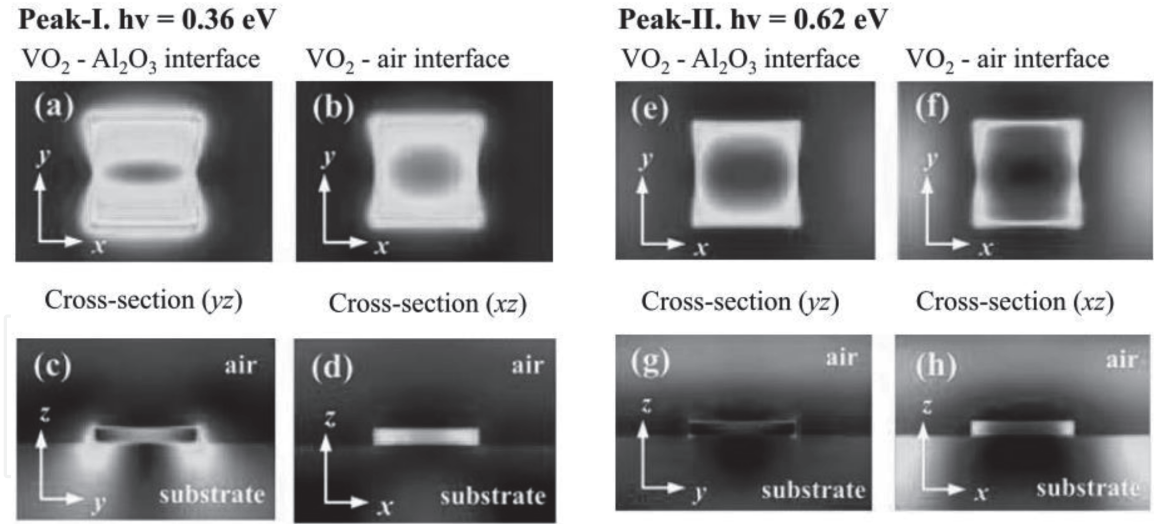

Figure 2.
(a) Temperature-dependent Raman spectra of the 600-nm nanodot array. (b) Hysteresis curve of the ω_o Raman active peak. Closed and open dots represent heating and cooling processes of the sample, respectively. 2D Raman images taken at (c) 30°C and (d) 75°C.
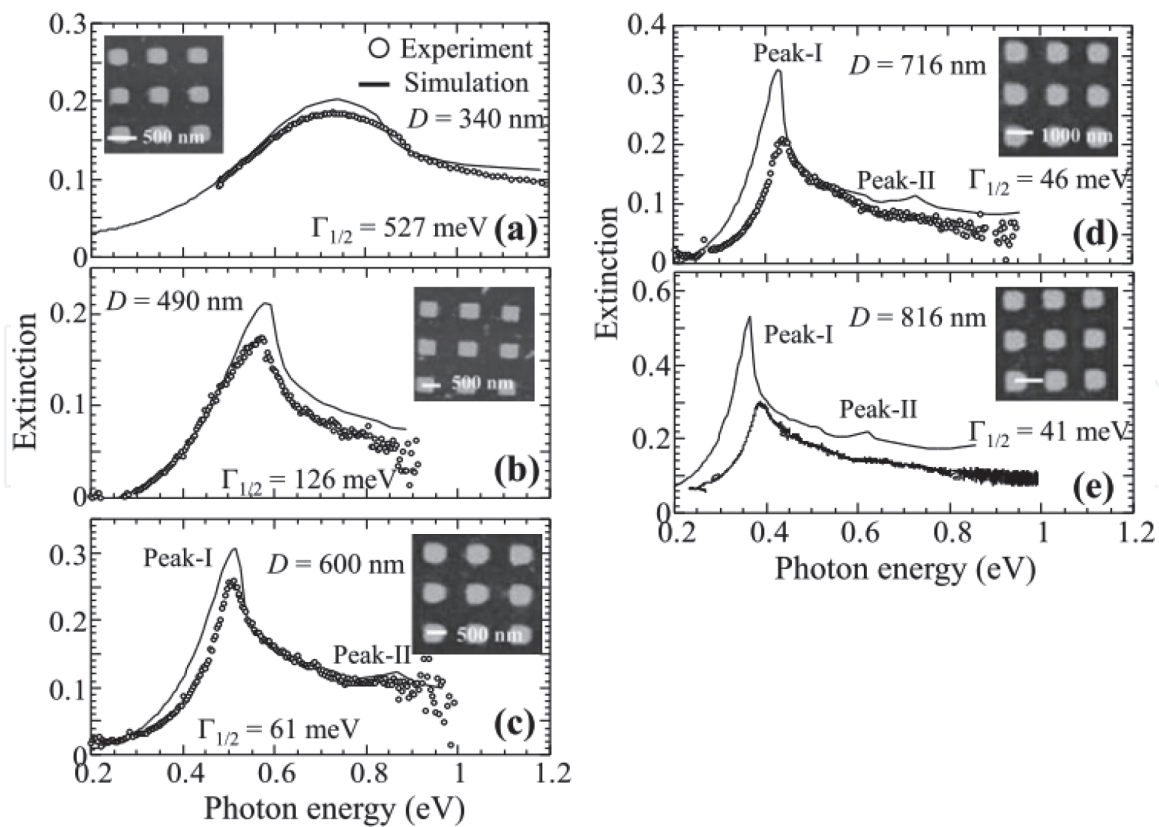
Figure 3.
Extinction (A) spectra and atomic force microscopy (AFM) images of nanodot arrays with different sizes [D = 340 (a), 490 (b), 600 (c), 716 (d), and 816 nm (e)]. Experimental and simulated spectra are represented by black lines and open circles, respectively [24].

nanodot size was checked using atomic force microscopy (AFM). The extinction spectrum of a $D = 340$ nm sample provided a broad spectral linewidth. However, the spectral linewidth gradually decreased with increasing nanodot size. The increase in nanodot size resulted in a red shift of the plasmon resonance to low photon energy, relating to long-range plasmon coupling based on the far-field since near-field interactions at a short range result in a blue shift of the resonance peak with increasing nanodot size [27]. Additionally, the experimental behavior was also observed with the simulated data using rigorous coupled-wave analysis (RCWA) (black lines in **Figure 3**). The magnitudes of the experimentally observed resonances were weaker than the simulated resonances, which may be a result of fabrication-related imperfections such as rounded edges and the corners of the nanodot arrays.

We could observe two kinds of resonance peaks (Peak-I and Peak-II) from the nanodot arrays with $D = 600$, 716 and 816 nm. Thereupon, we focused on the extinction of the nanodot array with $D = 816$ nm (**Figure 3e**), which showed Peak-I and Peak-II at 0.36 and 0.62 eV, respectively. The origin of the resonant peaks was clarified from three-dimensional field distributions based on the RCWA analysis. Simulations of the electric field (E-field) distributions were performed at 0.36 and 0.62 eV (**Figure 4**). The top-view E-fields at 0.36 eV (Peak-I) were enhanced at both interfaces between the nanodot and the substrate (substrate side), and between the nanodot and air (air side) (**Figure 4a, b**). The cross-section E-field revealed that the field intensity was more strongly concentrated on the substrate side than on the air side (**Figure 4c, d**), which showed a dipole plasmon resonance. On the other hand, the E-field at 0.62 eV (Peak-II) also emerged at both the substrate and air sides (**Figure 4e, f**), which was predominantly higher than that on the substrate side (**Figure 4g, h**). Therefore, the E-field at the substrate side adjacent to the substrate increased, and the field at the air side decreased. This behavior

Peak-I. hv = 0.36 eV

VO₂ - Al₂O₃ interface   VO₂ - air interface

(a)   (b)

Cross-section (*yz*)   Cross-section (*xz*)

(c)   (d)

Peak-II. hv = 0.62 eV

VO₂ - Al₂O₃ interface   VO₂ - air interface

(e)   (f)

Cross-section (*yz*)   Cross-section (*xz*)

(g)   (h)

Figure 4.
Electric fields (E-field) of the nanodot array (D = 816 nm) calculated at resonances of 0.36 eV (upper images: Peak-I) and 0.62 eV (lower images: Peak-II). (a) and (e) show in-plane (x-y) field distributions at VO₂-Al₂O₃ interfaces at 0.36 eV and 0.62 eV, respectively. In-plane (x-y) field distributions of VO₂-air interfaces at 0.36 and 0.62 eV are exhibited in (b) and (f), respectively. (c) and (g) indicate cross-section (z-y) field distributions at 0.46 and 0.62 eV, respectively. Cross-section (z-x) field distributions at 0.36 and 0.62 eV are indicated in (d) and (h), respectively.
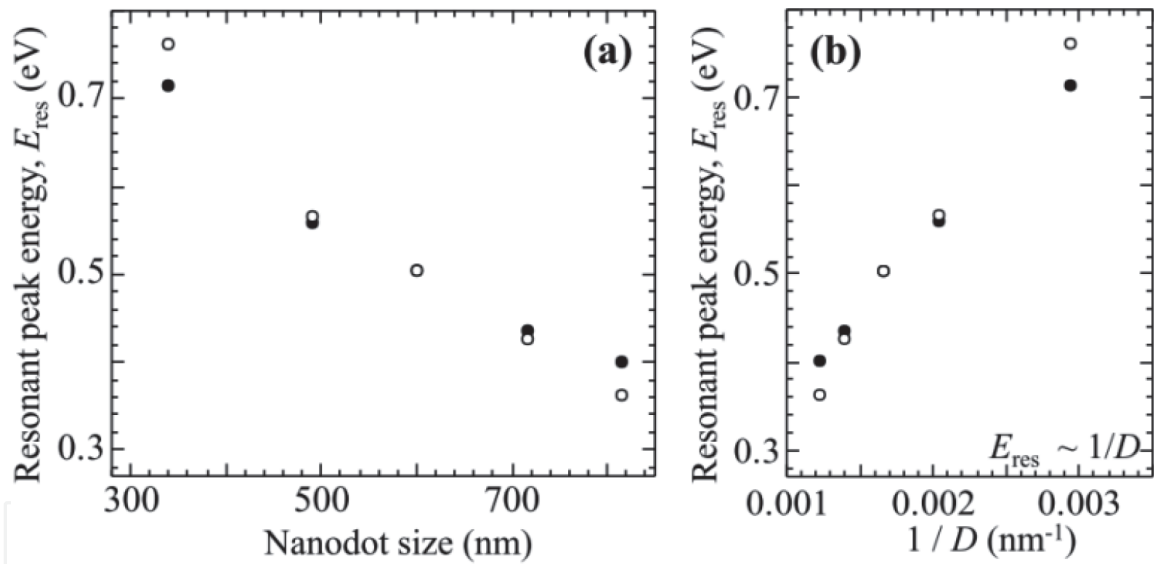
Figure 5.
(a) Energy positions of resonant peaks of Peak-I as a function of nanodot array. Experimental and simulated peaks are indicated by open and closed circles, respectively. (b) Scaling of the resonant peak energy (E_res) with inverse nanodot size (1/D) [24].

was consistent with the loss of symmetry following introduction of a substrate. The overall field distribution was weighted toward the lower edge in the vicinity of the substrate and toward the top edge away from the substrate. This phenomenon is attributed to substrate-induced plasmon hybridization for a metallic nanostructure on a dielectric substrate [28]. The dominant resonance of Peak-I, which is the focus of this study, mainly reflects the *E*-field between the nanodot and the substrate. This *E*-field provides the collective plasmon resonance in the nanodot arrays.

2.3 Damping processes

Figure 5a shows the relationship between nanodot size and resonant peak energy. The experimental and simulated data showed that a dominant peak energy

DOI: http://dx.doi.org/10.5772/intechopen.91215

(E_{res}) associated with the dipolar resonance exhibited spectral red shifting with increasing nanodot size.

Besides, E_{res} was inversely proportional to $1/D$ (**Figure 5b**), which indicated that dynamic polarization effectively reduced the number of electrons oscillating coherently, and shifted the resonance energy into the low photon energy.

Figure 6a shows the spectral linewidth (Γ: FWHM) as a function of resonant peak energy (E_{res}). We extracted the spectral linewidth ($\Gamma = 2\Gamma_{1/2}$) as the red half-width at half-maximum $\Gamma_{1/2} = E_{res} - E_{1/2}$, where $E_{1/2}$ is the photon energy for which the extinction is half of the peak value [29]. The experimentally obtained Γ was systematically small with decreasing resonant energy, and was close to that of the simulated data. Plasmon quality ($Q = E_{res}/\Gamma$) enhanced with a reduction in resonant peak energy (**Figure 6b**). The slight difference in Γ between experimental and simulated data gradually increased with decreasing nanodot size. This may be related to surface damage of the nanodot owing to a side etching effect in the SF_6 plasma process.
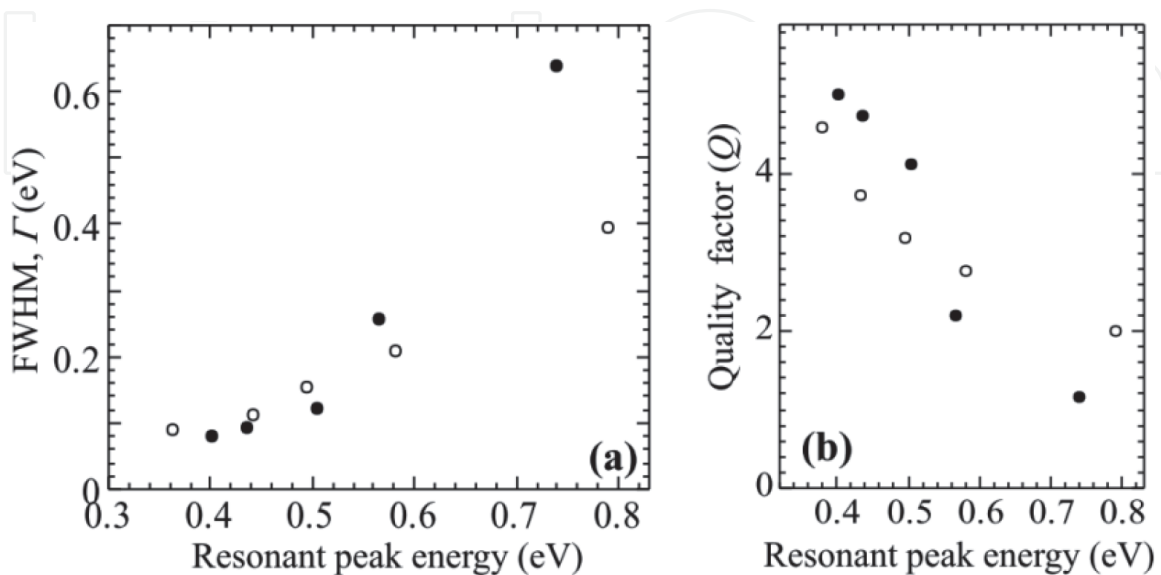
The relationship between spectral linewidth and resonant energy is related to the dielectric functions of VO_2. **Figure 7a** shows complex dielectric functions of metallic VO_2 epitaxial films prior to nanofabrication. We discuss the plasmonic response of metallic VO_2 nanodots on the basis of bulk dielectric functions. The energy-dependent scattering rate (γ^*) and effective mass (m^*) are important factors in clarifying the damping mechanism, as estimated using the extended Drude model [30, 31].

$$\varepsilon(\omega) = \varepsilon_\infty - \frac{\omega_p^2}{\omega[\omega + i\gamma^*]} \tag{1}$$

where ε_∞ represents the high-energy dielectric constant derived from interband transitions. We used $\varepsilon_\infty = 9$. ω_p is the plasma frequency defined as follows [30, 31]: $\omega_p^2 = 4\pi N e^2 / m^*(\omega)$ „ where N_e is the total density of conduction electrons.
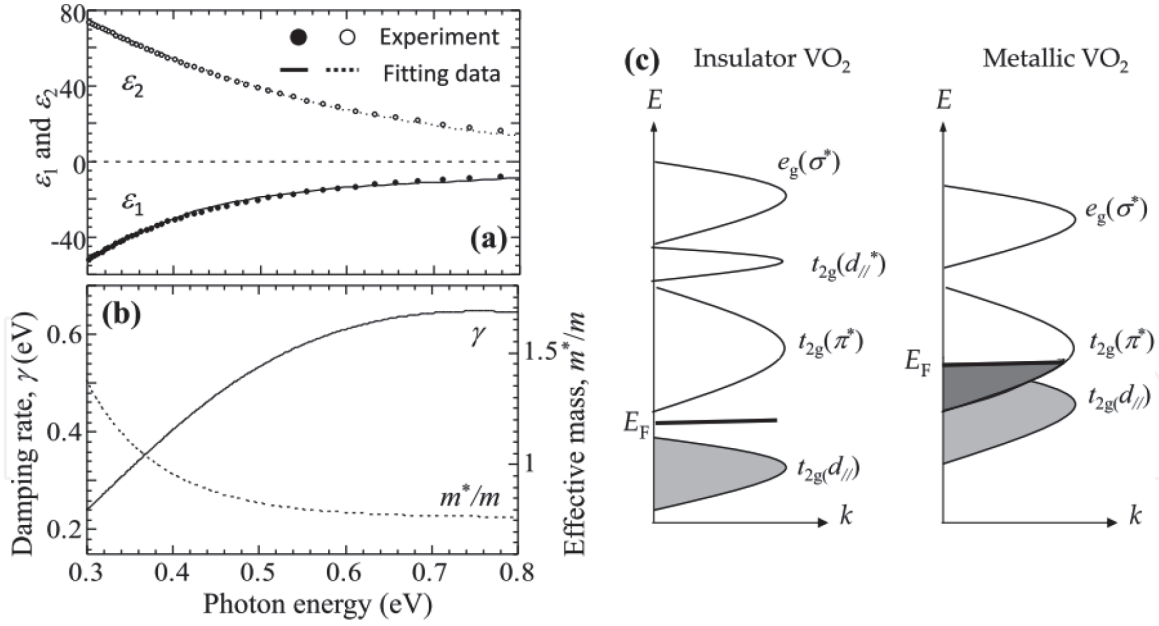
$$m(\omega)^* = \frac{4\pi e^2 N_e \gamma^*}{\varepsilon_2 \omega(\omega^2 + \gamma^{*2})} \tag{2}$$

$$\gamma(\omega)^* = \frac{\omega \varepsilon_2}{(\varepsilon_\infty - \varepsilon_1)} \tag{3}$$

Figure 6.
(a) Plasmon linewidth (Γ) obtained from experimental (closed circles) and simulated (open circles) results as a function of resonant peak energy. Inset indicates an extinction spectrum of the nanodot array with D = 816 nm. (b) Plasmon quality (Q = ℏ/Γ) as a function of E_{res} [24].

Figure 7.
(a) Real (ε_1: closed dots) and imaginary (ε_2: open dots) parts of the dielectric function in a VO_2 film prior to nanofabrications. Note that energy-dependent ε_1 and ε_2 in a VO_2 film were used since size-dependent plasmon damping is neglected. (b) Damping rate (γ^*: Straight line) and effective mass (m^*/m: dotted line) as a function of photon energy. (c) Schematic representation of electronic band structures of insulating and metal VO_2 [24].

ε_1 and ε_2 indicate the real and imaginary parts of the dielectric function, respectively, when we define $\varepsilon(\omega) = \varepsilon_1(\omega) + i\varepsilon_2(\omega)$. Based on an N_e value of 5.2×10^{22} cm^{-3} from a Hall measurement, the energy-dependent γ^* and m^*/m_0 (m_0 is the electronic band mass) in metal VO_2 were extracted (**Figure 7b**). In the simple Drude model, the scattering rate is considered independent of the photon energy. However, $\gamma(\omega)$ actually increased with increasing photon energy. The energy-dependent scattering rate is generally based on electron-electron (*e-e*) scattering and electron-phonon (*e-ph*) scattering. The behavior of $\rho(\omega)$ was proportional to ω^2, which indicated that the scattering rate of metal VO_2 was dominated by *e-e* scattering. Additionally, m^*/m_0 was enhanced slightly at a lower photon energy below 0.4 eV, which is characteristic of a Mott insulator [32]. Results showed that the energy-dependent Γ of plasmonic resonance was correlated with the energy-dependent γ in the extended Drude model. A plasmonic linewidth is mainly the sum of three separate processes involving intraband, interband, and radiative contributions (we ignore electron-surface damping, and chemical interface damping) [33]. The electronic band structure of VO_2 is explained as follows [34]. The crystal field splits degenerate 3*d*-orbitals into t_{2g} and e_g bands. The t_{2g} bands further split into $t_{2g}(d_{//})$ and $t_{2g}(\pi^*)$ bands. A $t_{2g}(d_{//})$ band splits into the upper $t_{2g}(d_{//}^*)$ and lower $t_{2g}(d_{//})$ bands in insulator VO_2. In metallic VO_2, an $t_{2g}(d_{//})$ band overlaps with an $t_{2g}(\pi^*)$ band at E_F, consisting only of 3*d* orbitals (**Figure 7c**). Additionally, radiation contribution to the plasmon damping was relatively small in this work since the plasmon linewidths gradually decreased with increasing nanodot size. As a consequence, intraband damping related to *e-e* scattering in the conduction band plays an important role in determining the plasmon linewidth, which is derived from the highly corrected electron system of VO_2.

3. Optical dynamics

Near-infrared laser pulses ranging from 1.9 to 2.5 μm were realized from a single supercontinuum pulse by intrapulse difference-frequency mixing with a spectral

focusing scheme. For our pump and probe system, the probe wavelength was the same as that of the pump.

Details regarding the generation of femtosecond laser pulses (pulse width $\sim$ 150 fs) are described in [35].

We initially investigated differential transmittance ($\Delta T/T$) signals as a function of laser influence strength (P) (**Figure 8a**). $\Delta T/T$ can be defined as $\Delta T/T = (T_{on} - T_{off})/T_{off}$, with T_{on} and T_{off} being the probe signals reflected by the excited and unperturbed samples, respectively. An excitation wavelength of λ = 2.1 μm was used. The VO_2 nanodot array with D = 490 nm was used as a measurement sample. The sample temperature was maintained at 90°C to retain metallic state of VO_2. $\Delta T/T$ showed negative responses under different laser influence strengths (P = 100–560 mJ/cm^2), which indicated an increase in photo-induced absorbance. As shown in **Figure 8a**, the plasmon dynamics obey a well-known process [36]: carrier dephasing; electron-electron (*e-e*) scattering [process (1)], determined in the rise time, carrier cooling and lattice heating by electron-phonon (*e-ph*) scattering [process (2)], and followed by cooling of the lattice based on dissipation of phonons into the environment [process (3), photon-phonon (*ph-ph*) relaxation]. The optical dynamics of VO_2 nanodot arrays were mainly dominated by *e-e* and *e-ph* scattering processes in the plasmon relaxations. The rising (*e-e* scattering) and decay (*e-ph* scattering) time constants remained unchanged with different influence strengths, and were approximately 200 and 240 fs, respectively. The rising and decay processes could be described by a single exponential decay model. Besides, all $\Delta T/T$ signals were conducted below 1 ps, which differed from that employed for the noble metals [36]. The $\Delta T/T$ signals on silver and gold nanoparticles have commonly been extended in the range 10–20 ps [37]. Therefore, *e-e* and *e-ph* scattering on the VO_2 nanodot array was faster than that on the noble metals, contributing to optical modulations at the sub-picosecond scale. By contrast, *ph-ph* relaxation increased with increasing laser influence strength due to an increase in thermal relaxation.
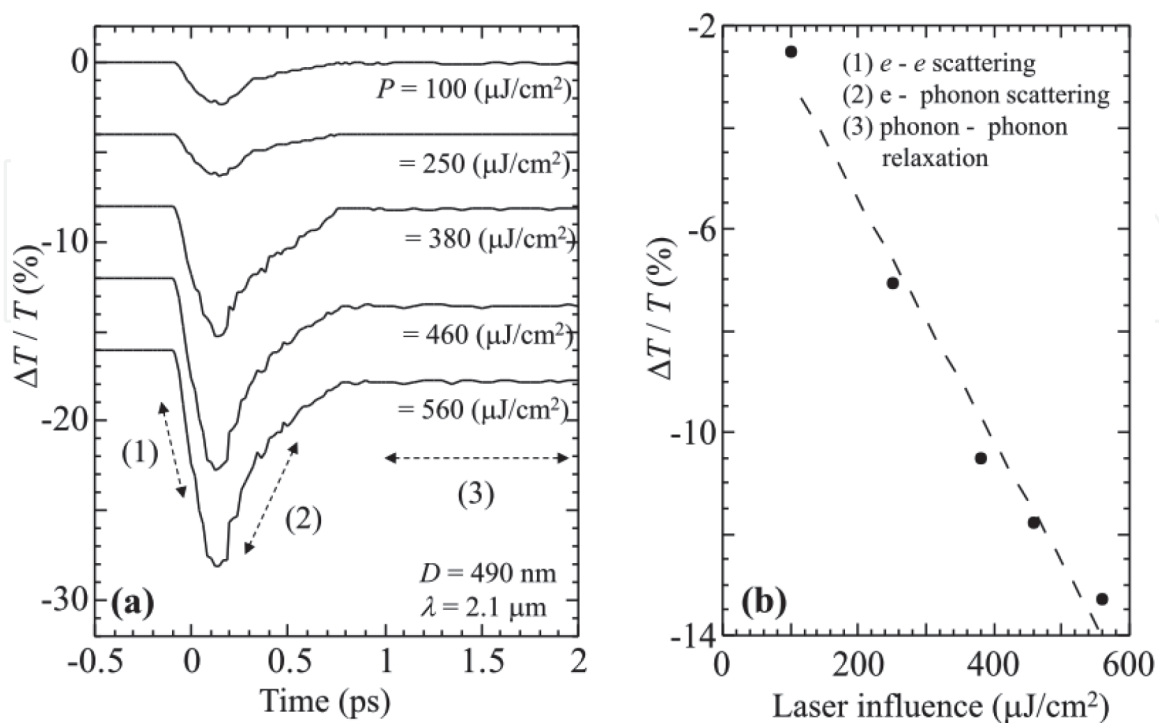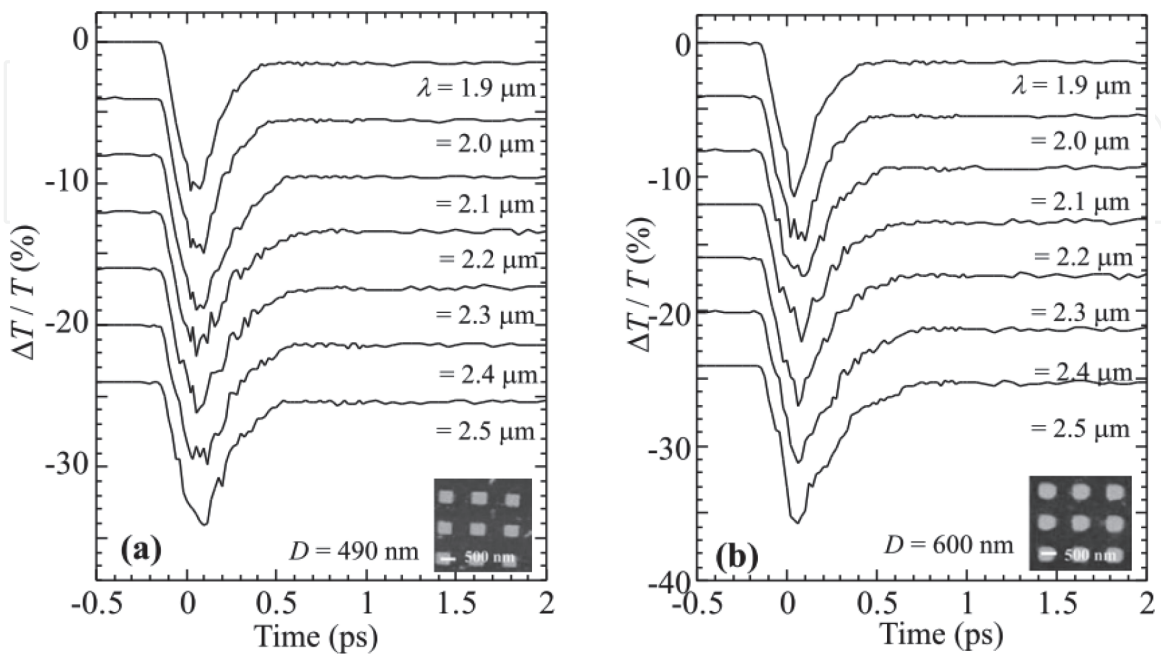

Figure 8.
(a) Differential transmittance (ΔT/T) signals as a function of lower influence strength. (1), (2), and (3) indicate e-e *scattering,* e-ph *scattering and* ph-ph *relaxation, respectively. (b) Dependence of ΔT/T on laser influence strength.*

The value of $\Delta T / T$ was inversely proportional to the laser influence strength (**Figure 8b**). No non-linear response was found within these laser influences.

On the other hand, no carrier dephasing was observed. The relaxation time of carrier dephasing is characterized by the time constant, T_2, which is related to the time constant for inelastic decay of the plasmon population, T_1, via $T_2^{-1} = T_1^{-1} / 2 + T^{*-1}$, where T^* represents possible elastic phase-loss processes [38]. We can estimate T_2 using the following relation: $T_2 = 2\hbar / \Gamma$, where $\hbar$ and Γ ($= 2\Gamma_{1/2}$) indicate the Plank constant and spectral linewidth, respectively. In the case of $D = 490$ nm, T_2 was estimated to be 5.1 fs, which was below the measurement limit.

Figure 9a shows differential transmittance signals as a function of laser wavelength for VO$_2$ nanodot arrays with $D = 490$ nm, revealing that the decay time of $\Delta T / T$ signals was dependent on laser wavelength. The decay time could be well fitted by a single exponential component in all laser wavelengths, as shown in **Figure 10a**. Photon energy-dependent plasmon lifetimes were extracted from decay times of $\Delta T / T$ signals. Lifetimes gradually increased with decreasing photon energy, and showed a maximum value ($\sim$0.257 ps) at 0.57 eV. The dependence of lifetime on photon energy was close to that on extinction. Similar results were obtained on the nanodot array with $D = 600$ nm (**Figures 9b** and **10b**). That is, the longest lifetimes were observed using laser wavelengths at the plasmon resonance peaks.

The extinction spectra of VO$_2$ nanodot arrays are characterized by the presence of plasmon bands in the IR range. The surface plasmon is a quantum of $h / (2\pi\omega_p)$ of plasma oscillation. The plasmon bands of VO$_2$ nanodot arrays were attributed to dipole oscillations of the free carriers (electrons) in the C.B. occupying the energy states immediately above the Fermi energy. The band structure of metallic VO$_2$ is more complex compared with oxide semiconductors (**Figure 7c**). The Fermi level is located in the $t_{2g}(\pi^*)$ level, which is partially overlapped with the $t_{2g}(d_{//})$ level. The optical excitations of metallic VO$_2$ comprised the three interband transitions E_1, E_2, and E_3 that were observed at around $\sim$1.22, $\sim$3.37, and $\sim$5.90 eV, respectively [39]. In particular, the lowest optical transition E_1 corresponds to optical excitation from the filled $t_{2g}(d_{//})$ to empty $t_{2g}(\pi^*)$ bands. This band transition broadly exists in the range 0.5–2 eV, which is closely related to the plasmon dynamics.
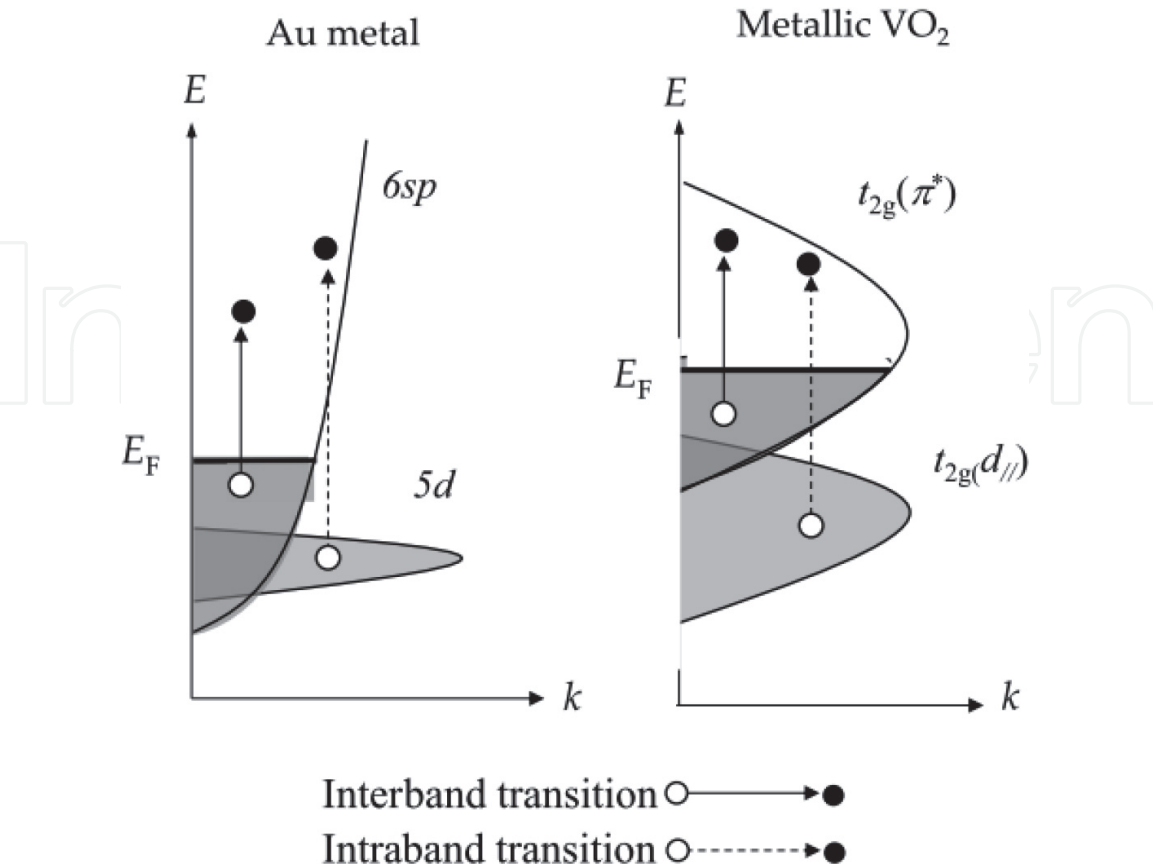

Figure 9.
Differential transmittance signals as a function of laser wavelength for VO$_2$ nanodot arrays with (a) D = 490 nm and (b) D = 600 nm.
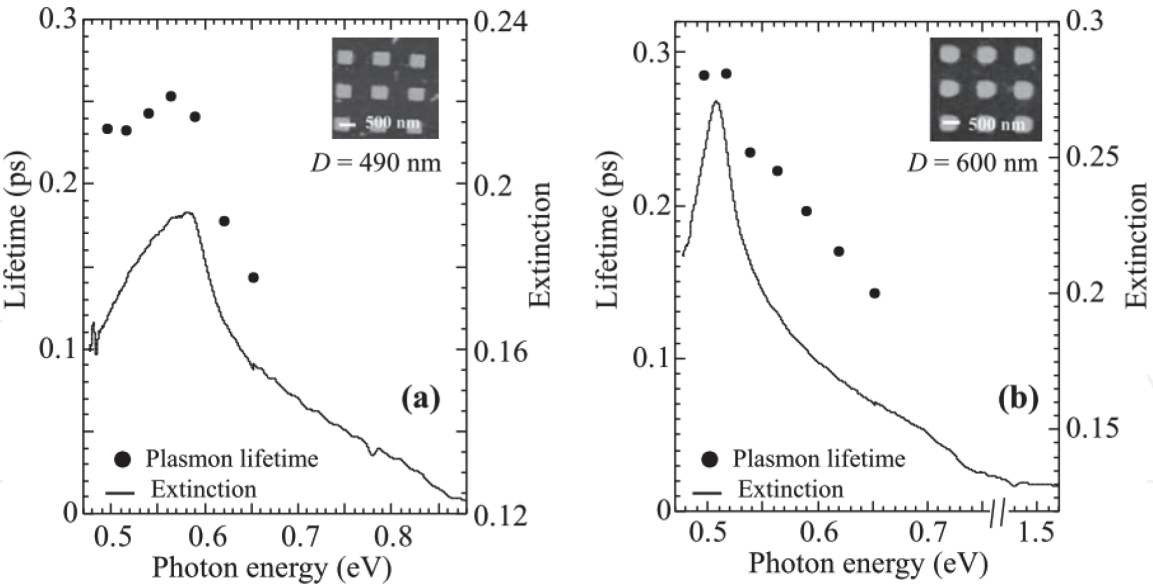
Figure 10.
Relationship between plasmon lifetime and extinction as a function of photon energy for VO$_2$ nanodot arrays with (a) D = 490 nm and (b) D = 600 nm.

In general, it is known that plasmon lifetimes differ largely between interband and intraband excitations. For an Au metal, the *s* band of the C.B. is overlapped with the *d* band, which provides two optical transitions as follows [40]. The interband excitations from *d* to *s* bands result in short-lived lifetimes due to the bounded carriers. By contrast, the intraband excitations in the C.B. consisting of the *6sp* bands are composed of free carriers, leading to long-lived lifetimes as compared to the interband excitations (**Figure 11a**). On the other hand, for VO$_2$, the $t_{2g}(\pi^*)$ band is partially combined with the $t_{2g}(d_{//})$ band existing in VO$_2$ in addition to the

Figure 11.
The electronic band structures of Au metal (left) and metallic VO$_2$ (right).

intraband excitation within the $t_{2g}(\pi^*)$. That is, the long-lived lifetimes of plasmon peaks at 0.56 and 0.51 eV for nanodot arrays with D = 490 and 600 nm, respectively, were due to intraband excitations of free carriers in the C.B., which provided longer lifetimes than those of interband excitations. Optical dynamics of VO_2 were influenced by the intraband and interband transitions. The plasmon lifetimes were determined by the intraband excitations in the C.B., which were attributed to the band structure of VO_2.

4. Summary

We investigated infrared plasmonic responses of VO_2 nanodot arrays and their optical modulations. Comparison of the experimental plasmon resonances with electromagnetic simulations enabled us to perform spectral assignments and field distributions. In particular, plasmon coupling between metallic VO_2 nanodots contributed to the collective excitation mode. Plasmon damping of VO_2 was closely related to the specific band structure, which affected the optical dynamics. The plasmonic excitations excited by the fs pulse lasers showed ultrafast optical responses at the sub-picosecond scale, which were dependent on laser wavelength. The optical excitations of VO_2 comprised intraband and interband transitions. The long-lived lifetimes were observed at the resonant peaks in terms of free carrier excitations of VO_2. This result was attributed to the band structure, which affected the plasmon lifetimes.

Author details

Hiroaki Matsui[1,2]

1 Department of Bioengineering, The University of Tokyo, Bunkyo-ku, Tokyo, Japan

2 Department of Electrical Engineering and Information Systems, The University of Tokyo, Bunkyo-ku, Tokyo, Japan

*Address all correspondence to: hiroaki@ee.t.u-tokyo.ac.jp

IntechOpen

References

[1] Matsui H, Furuta S, Tabata H. Mint: Role of electron carriers on local surface plasmon resonances in dope oxide semiconductor nanocrystals. Applied Physics Letters. 2014;**104**:211903. DOI: 10.1063/1.4880356

[2] Matsui H, Badalawa H, Hasebe T, Furuta S, Nomura W, Yatsui T, et al. Mint: Coupling of Er light emissions to plasmon modes on In_2O_3:Sn nanoparticle sheets in the near-infrared range. Applied Physics Letters. 2014;**105**:041903. DOI: 10.1063/1.4892004

[3] Runnerstrom EL, Bergerud A, Agrawal A, Johns RW, Dahkman CJ, Singh A, et al. Mint: Defect engineering in plasmonic metal oxide nanocrystals. Nano Letters. 2016;**16**:3390-3398. DOI: 10.1021/acs.nanolett6b01171

[4] Hsu SW, Ngo C, Tao AR. Mint: Tunable and directional plasmonic coupling within semiconductor nanodisk assemblies. Nano Letters. 2014;**14**: 2372-2380. DOI: 10.1021/nl404777h

[5] Palomaki PK, Miller EM, Neale NR. Mint: Control of plasmonic and interband transitions in colloidal indium nitride nanocrystals. Journal of the American Chemical Society. 2013;**135**: 14142-14150. DOI: 10.1021/ja404599g

[6] Naik CV, Shalaev VM, Boltasseva A. Mint: Alternative plasmonic materials: Beyond gold and silver. Advanced Materials. 2013;**25**:3264-3294. DOI: 10.1002/adma20125076

[7] Pattathil P, Giannuzzi R, Manca M. Mint: Self-powered NIR-selective dynamic windows based on broad tuning of the localized surface plasmon resonance in nanoporous ITO electrodes. Nano Energy. 2016;**30**:242-251. DOI: 10.1016/j.nanoen.2016.10.013

[8] Dahlman C, Agrawal A, Staller CM, Adair J, Milliron DJ. Mint: Anisotropic origins of localized surface plasmon resonance in n-type anatase TiO_2 nanocrystals. Chemistry of Materials. 2019;**31**:502-511. DOI: 10.1021/acs.chemmater.8b04519

[9] Kim DH, Kwok HS. Mint: Pulsed laser deposition of VO_2 thin films. Applied Physics Letters. 1994;**65**: 3188-3190. DOI: 10.1063/1.112476

[10] Basov DN, Averitt RD, Marel D, Deressel M, Haule K. Mint: Electrodynamics of correlated electron materials. Reviews of Modern Physics. 2011;**83**:471-541. DOI: 10.1103/RevModPhys.83.471

[11] Kanki T, Hotta Y, Asakawa N, Kawai T, Tanaka H. Mint: Noise-driven signal transmission using nonlinearity of VO_2 thin films. Applied Physics Letters. 2010;**96**:242108. DOI: 10.1063/1.3455335

[12] Bae SH, Lee S, Lin L, Jo BH, Park C, Wang ZL. Mint: The memristive properties of a single VO_2 nanowire with switching controlled by self-heating. Advanced Materials. 2013;**25**:5098-5103. DOI: 10.1002/adma.201302511

[13] Zhang Z, Gao Y, Chen Z, Du J, Cao C, Kang L, et al. Mint: Thermochromic VO_2 thin films: Solution-based processing, improved optical properties, and lowered phase transformation temperature. Langmuir. 2010;**26**:10738-10744. DOI: 10.1021/la100515k

[14] Ke Y, Wen X, Zhao D, Che R, Xiong Q, Long Q. Mint: Controllable fabrication of two-dimensional patterned VO_2 nanoparticle, nanodome, and nanonet arrays with tunable temperature-dependent localized surface plasmon resonance. ACS Nano. 2017;**11**:7542-7551. DOI: 10.1021/acsnano.7b02232

[15] Zhu Z, Evans PG, Haglund RF Jr, Valentine JG. Mint: Dynamically

reconfigurable metadevice employing nanostructured phase-change materials. Nano Letters. 2017;**17**:4881-4885. DOI: 10.1021/acs.nanolett7b01767

[16] Appavoo K, Wang B, Seo M, Nag J, Prasankumar RP, Hilton DJ, et al. Mint: Ultrafast phase transition via catastrophic phonon collapse driven by plasmonic hot-electron injection. Nano Letters. 2014;**14**:1127-1133. DOI: 10.1021/nl4044828

[17] Zhu J, Huang A, Ma H, Ma Y, Tong K, Ji S, et al. Mint: Composite film of vanadium dioxide nanoparticles and ionic-nickel-chlorine complexes with excellent visible thermochromic performance. ACS Applied Materials & Interfaces. 2016;**43**:29742-29748. DOI: 10.1021/acsami.6b112020

[18] MacDonald KF, Sáimon ZL, Stockman MI, Zheludev NI. Mint: Ultrafast active plasmonics. Nature Photonics. 2009;**3**:55-58. DOI: 10.1038/NPHOTON.2008.249

[19] Harutyunyan H, Martinson ABF, Rosenmann D, Khorashad LK, Besteiro LV, Govorov AO, et al. Mint: Anomalous ultrafast dynamics of hot plasmonic electrons in nanostructures with hot spots. Nature Nanotechnology. 2015;**10**:770-775. DOI: 10.1038/NNANO2015.165

[20] Hodak JH, Martini I, Hartland GV. Mint: Spectroscopy and dynamics of nanometer-sized noble metal particles. Journal of Physical Chemistry B. 1998;**102**:6958-6967. DOI: 10.1021/jp9809787

[21] Guo P, Schaller RD, Ketterson JB, Chang RPH. Mint: Ultrafast switching of tunable infrared plasmons in indium tin oxide nanorod arrays with large absolute amplitude. Nature Photonics. 2016;**10**:267-273. DOI: 10.1038/NPHOTON.2016.14

[22] Calzolari A, Ruini A, Catellani A. Mint: Transparent conductive oxides as near-IR plasmonic materials: The case of Al-doped ZnO derivatives. ACS Photonics. 2014;**1**:703-709. DOI: 10.1021/ph500118y

[23] Diroll RT, Chang RPH, Schaller RD. Mint: Large transient optical modulation of epsilon-near-zero colloidal nanocrystals. ACS Nano. 2016;**10**: 10099-10105. DOI: 10.1021/acsnano.6b05116

[24] Matsui H, Ho YL, Kanki T, Tanaka H, Delaunay JJ, Tabata H. Mint: Mid-infrared plasmonic resonances in 2D VO$_2$ nanosquare arrays. Advanced Optical Materials. 2015;**3**:1759-1767. DOI: 10.1002/adom.201500322

[25] Atkin JM, Berweger S, Chavez EK, Raschke MB, Cao J, Fan W, et al. Mint: Strain and temperature dependence of the insulating phases of VO$_2$ near the metal-insulator transition. Physical Review B. 2012;**85**:02010(R). DOI: 10.1103/PhysRevB.85.020101

[26] Zhang S, Chou JY, Lauhon LJ. Mint: Direct correlation of structural domain formation with the metal insulator transition in a VO$_2$ nanobeam. Nano Letters. 2009;**9**:4527-4532. DOI: 10.1021/nl9028973

[27] Appavoo K, Lei DY, Sonnefraud Y, Wang B, Pantelides ST, Maier SA, et al. Mint: Role of defects in the phase transition of VO$_2$ nanoparticles probed by plasmon resonance spectroscopy. Nano Letters. 2012;**12**:780-786. DOI: 10.1021/nl203782y

[28] Zhang S, Bao K, Halas NJ, Xu H, Nordlander P. Mint: Substrate-induced Fano resonances of a plasmonic nanocube: A rote to increased-sensitivity localized surface plasmon resonance sensors revealed. Nano Letters. 2011;**11**:1657-1663. DOI: 10.1021/nl200135r

[29] Berciaud S, Cognet L, Tamarat P, Lounis B. Mint: Observation of intrinsic

size effects in the optical response of individual gold nanoparticles. Nano Letters. 2005;**5**:515-518. DOI: 10.1021/nl050062t

[30] Choi HS, Ahn JS, Jung JH, Noh TW, Kim DH. Mid-infrared properties of a VO_2 film near the metal-insulator transition. Physical Review B. 1996;**54**:4621-4628. DOI: 10.1003/PhysRevB.54.4621

[31] Makino H, Inoue IH, Rozenberg MJ, Hase I, Aiura Y, Onari S. Mint: Bandwidth control in a perovskite-type 3d—correlated metal $Ca_{1-x}Sr_xVO_3$. II. Optical spectroscopy. Physical Review B. 1998;**58**:4384-4393. DOI: 10.1003/PhysRevB.58.4384

[32] Okazaki K, Sugai S, Muraoka Y, Hiroi Z. Mint: Role of electron-electron and electron-phonon interaction effects in the optical conductivity of VO_2. Physical Review B. 2006;**73**:165116. DOI: 10.1103/PhysRevB.73.165116

[33] Hu M, Novo C, Funston A, Wang H, Staleva H, Zou S, et al. Mint: Dark-field microscopy studies of single metal nanoparticles: Understanding the factors that influence the linewidth of the localized surface plasmon resonance. Journal of Materials Chemistry. 2008;**18**:1949-1960. DOI: 10.1039/B714759G

[34] Qazilbash MM, Schafgans AA, Burch KS, Yun SJ, Chae BG, Kim J, et al. Mint: Electrodynamics of the vanadium oxides VO_2 and V_2O_3. Physical Review B. 2008;**77**:115121. DOI: 10.1103/PhysRevB.77.115121

[35] Yamaguchi Y, Hida R, Suzuki T, Isa F, Yoshikiyo K, Fujii L, et al. Mint: Shaping and amplification of wavelength-tunable mid-infrared femtosecond pulses generated by intra-pulse difference-frequency mixing with spectral focusing. Journal of the Optical Society of America B. 2018;**35**:C1. DOI: 10.1364/JOSAB.35.0000C1

[36] Arbouet A, Voisin C, Christofilos D, Langot P, Del Fatti N, Vallée F, et al. Electron-phonon scattering in metal clusters. Physical Review Letters. 2003;**90**:177401. DOI: 10.1103/PhysRevLett.90.177401

[37] Link S, Burda C, Wang ZL, El-Sayed MA. Electron dynamics in gold and gold-silver alloy nanoparticles: The influence of a nonequilibrium electron distribution and the size dependence of the electron-phonon relaxation. The Journal of Chemical Physics. 1999;**111**:1255-1265

[38] Sönnichsen C, Franzl T, Wilk T, Plessen G, Feldmann J. Mint: Drastic reduction of plasmon damping in gold nanorods. Physical Review Letters. 2002;**88**:077402. DOI: 10.1103/PhysRevLett.88.077402

[39] Zhang P, Jiang K, Deng Q, You Q, Zhang J, Wu J, et al. Mint: Manipulations from oxygen partial pressure on the higher energy electronic transition and dielectric function of VO_2 films during a metal-insulator transition process. Journal of Materials Chemistry C. 2015;**3**:5033-5040. DOI: 10.1039/c5tc00002e

[40] Hartland GV. Mint: Optical studies of dynamics in noble metal nanostructures. Chemical Reviews. 2011;**111**:3858-3887. DOI: 10.1021/cr1002547